PSR J1709-4429's Proper Motion and Its Relationship to SNR G343.1–2.3

Martijn de Vries[1] ⬡, Roger W. Romani[1] ⬡, Oleg Kargaltsev[2] ⬡, George Pavlov[3], Bettina Posselt[3,4], Patrick Slane[5] ⬡,
Niccolo' Bucciantini[6] ⬡, C.-Y. Ng[7] ⬡, and Noel Klingler[8] ⬡

[1] Department of Physics/KIPAC, Stanford University, Stanford, CA 94305-4060, USA; mndvries@stanford.edu
[2] Department of Physics, George Washington University, Washington, DC 20052, USA
[3] Department of Astronomy & Astrophysics, Pennsylvania State University, University Park, PA 16802, USA
[4] Department of Physics, University of Oxford, OX1 3PU Oxford, UK
[5] Harvard-Smithsonian Center for Astrophysics, 60 Garden Street, Cambridge, MA 02138, USA
[6] INAF—Osservatorio Astrofisico di Arcetri, L.go Fermi 5, I-50125, Firenze, Italy
[7] Department of Physics, The University of Hong Kong, Pokfulam Road, Hong Kong
[8] Department of Astronomy and Astrophysics, The Pennsylvania State University, 525 Davey Laboratory, University Park, PA 16802, USA

Abstract

We have obtained a deep (670 ks) CXO ACIS image of the remarkable pulsar wind nebula (PWN) of PSR J1709 −4429, in four epochs during 2018–2019. Comparison with an archival 2004 data set provides a pulsar proper motion $\mu = 13 \pm 3$ mas yr^{-1} at a PA of $86° \pm 9°$ (1σ combined statistical and systematic uncertainties), precluding birth near the center of SNR G343.1−2.3. At the pulsar's characteristic age of 17 kyr, the association can be preserved through a combination of progenitor wind, birth kick, and PWN outflow. Associated TeV emission may, however, indicate an explosion in an earlier supernova. Inter-epoch comparison of the X-ray images shows that the PWN is dynamic, but we are unable to conclusively measure flow speeds from blob motion. The pulsar has generated a radio/X-ray wind bubble, and we argue that the PWN's long narrow jets are swept back by shocked pulsar wind venting from this cavity. These jets may trace the polar magnetic field lines of the PWN flow, an interesting challenge for numerical modeling.

1. Introduction

PSR J1709-4429 is a young ($\tau_c = P/2\dot{P} = 1.7 \times 10^4$ yr) pulsar, with spindown luminosity $\dot{E} \approx 4 \times 10^{36}$ erg s^{-1}, originally discovered by Johnston et al. (1992). At high energies, it was first observed with EGRET, making it one of the few known γ-ray pulsars at the time (McAdam et al. 1993). CXO observations in 2000 and 2004 revealed X-ray pulsations (Gotthelf et al. 2002). The excellent angular resolution of CXO also revealed the complex X-ray structure of the torus, equatorial outflow, and jets that appear to be swept back by the PSR motion (Romani et al. 2005). Fits to the torus and jets following the fitting procedure laid out by Ng & Romani (2004), yielded strong constraints on the position angle ($163°.6 \pm 0°.7$), inclination ($53.3^{+1.4}_{-1.6}$), and torus Doppler boosting factor ($\beta = 0.70 \pm 0.01$).

The nearby supernova remnant (SNR) G343.1−2.3, which is observed at radio wavelengths, has long been discussed as the possible PSR birthsite. The objects appear to be at similar distances: the SNR distance was estimated from the rather rough $\Sigma - D$ relationship to be ∼3 kpc (McAdam et al. 1993), while the dispersion measure (DM) distance of the PSR, according to the NE2001 model of Cordes & Lazio (2002), is $d \approx 2.3$ kpc. However, radio scintillation measurements by Johnston et al. (1998) suggest a low transverse velocity ≈90 km s^{-1}. At the spindown age of J1709, this velocity is too low by a factor of a few for the PSR to originate from the current center of the SNR.

More recently, observations with the the High Energy Stereoscopic System (H.E.S.S.) have shown an extended source of TeV emission west of the PSR (H.E.S.S. Collaboration et al. 2011). This TeV emission could be interpreted as inverse-Compton emission from electrons deposited during the pulsar's initial period of rapid spindown, cosmic rays generated by the SNR interacting with the surrounding interstellar medium, or some combination of both.

Measuring the direction and size of the proper motion vector should provide an important clue of whether the PSR, SNR, and TeV sources can be associated. However, this measurement has proven challenging with past observations. Romani et al. (2005) attempted to measure the proper motion using the CXO observations from 2000 and 2004, but these data proved to be insufficient for a proper motion detection. Radio VLBI astrometry has also been attempted, but proved infeasible with the Australian LBA, as there is no suitable in-beam reference source.

We have obtained 670 ks of new CXO observations between June 2018 and 2019. Combined with the archival observation from 2004, this gives us a 14.4 yr baseline allowing for direct astrometric measurement of the proper motion vector. The new data also show in more detail the pulsar wind bubble in which J1709 is embedded, and provide new constraints on the spectral properties of the emission in the PSR, torus, and jets.

2. Observations and Data Reduction

J1709 was observed with CXO for a total of 670 ks between 2018 June and 2019 June. Three of the observations in 2018 June were made with the ACIS-S array, while the rest use ACIS-I. Additionally, there are two archival observations, 15 ks in 2000 and 99 ks in 2004, described in more detail in Romani et al. (2005). A full overview of the observations is given in Table 1.

The data were processed with the standard CIAO reprocessing tools, using CIAO 4.12 and CALDB 4.9.1. An astrometric correction was applied to the data, by cutting out a $2' \times 2'$

Table 1
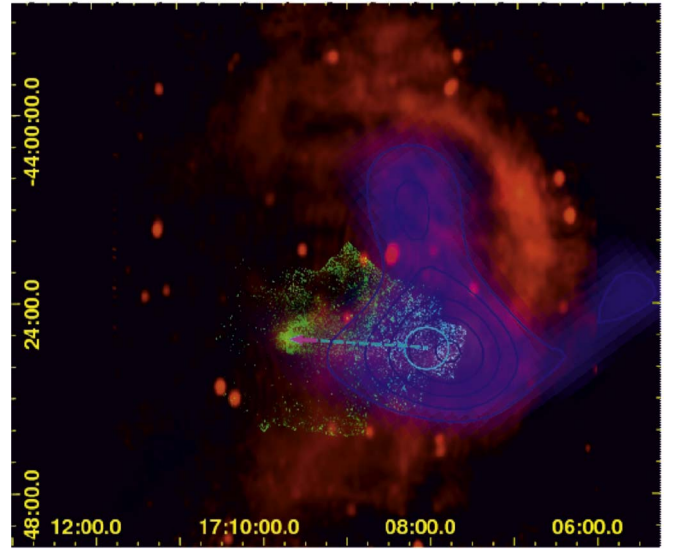Overview of J1709 CXO Observations Used in This Paper

Start Date (yyyy mm dd)	ObsID	Instrument	Exp (ks)	Θ (arcmin)
2000 08 14	757	ACIS-S	14.2	0′.4
2004 02 01	4608	ACIS-I	98.8	0′.6
2018 06 25	20300	ACIS-S	55.3	1′.0
2018 06 26	20299	ACIS-S	113.3	0′.8
2018 06 29	21109	ACIS-S	60.2	1′.0
2018 10 08	20302	ACIS-I	51.1	2′.4
2018 10 10	21871	ACIS-I	2.8	2′.4
2019 01 24	20303	ACIS-I	37.1	2′.6
2019 01 25	22060	ACIS-I	35.1	2′.6
2019 01 28	21899	ACIS-I	32.0	2′.6
2019 02 03	22075	ACIS-I	24.3	2′.6
2019 02 09	21869	ACIS-I	44.2	2′.6
2019 05 23	20301	ACIS-I	34.0	3′.0
2019 05 24	21870	ACIS-I	19.8	3′.0
2019 06 03	22244	ACIS-I	29.7	2′.9
2019 06 04	22005	ACIS-I	29.6	3′.0
2019 06 06	22246	ACIS-I	27.8	2′.9
2019 06 06	20304	ACIS-I	27.8	3′.0
2019 06 09	22245	ACIS-I	27.9	2′.9
2019 06 16	22087	ACIS-I	19.8	3′.0
Total			784.8	

Note. Θ indicates the distance in arcmin between the PSR and the on-axis position of the telescope.

Figure 1. Composite color image of J1709-4429 and the nearby SNR. Green: Chandra ACIS exposure-corrected 0.5-7 keV mosaic of all observations, smoothed (low exposure at the edges of the combined ACIS fields lead to poorly smoothed calibration artefacts). Blue with contours: H.E.S.S. TeV Galactic Plane Survey emission. Red: ATCA *L*-band (1.4 GHz) mosaic of SNR G343.1−2.3. The magenta arrow represents the PSR motion over its 1.7×10^4 yr spindown age (see Section 3); the cyan extension shows 5× this distance with an ellipse showing the 1σ proper motion uncertainty over this larger time span.
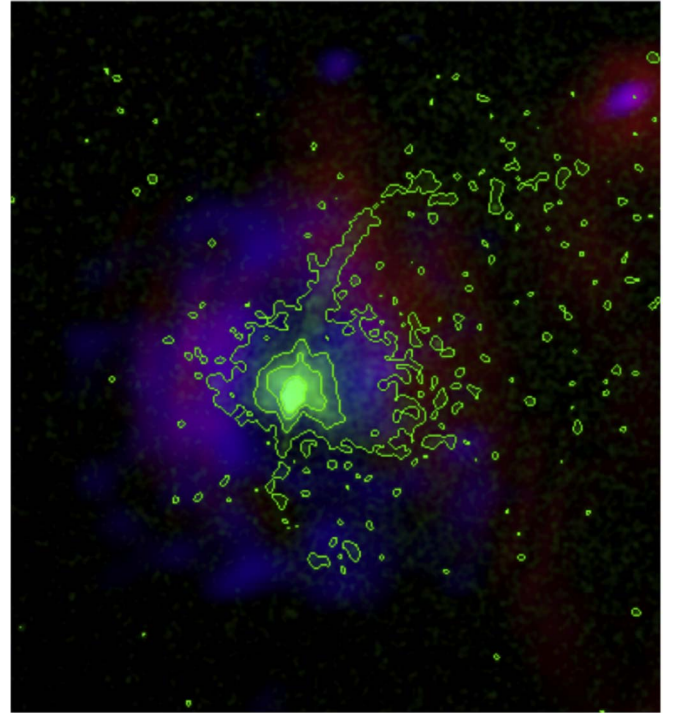
region centered on the PSR and outflow in each of the observations. We used ObsID 04608 as a reference observation because of its long exposure time, and reprojected the other ObsIDs onto the sky frame of the reference observation. Each of the ObsIDs were cross-correlated with the reference observation by shifting them in R.A. and decl. directions. The cross-correlation was then fit with a Lorentzian function to determine the coordinate offset, which was applied to the observation with the CIAO tool *wcs_update*. With this astrometry correction, all observations are approximately aligned on the PSR.

We created ACIS "blank-sky" background maps for each CCD of each observation, scaling them by the number of 10–12 keV counts of that observation. We also created instrument and exposure maps using the CIAO tools *mkinstmap* and *mkexpmap*, using an input spectrum extracted from the PWN and PSR as a whole. Using the event data, blank-sky backgrounds, and exposure maps, we created a background-subtracted, point-source-removed, exposure-corrected mosaic image by stacking all the observations.

Figure 1 shows the exposure-corrected X-ray image (using only pixels with 10% or more of the maximum exposure, green), overlaid with ATCA *L*-band (red, Dodson & Golap 2002), and the H.E.S.S. TeV Galactic plane survey data (blue, H.E.S.S. Collaboration et al. 2018). An arc of supernova remnant G343.1−2.3 is visible in the *L*-band data, while a ridge of radio emission extends from west to east, reaching the pulsar. The X-ray pulsar wind nebula shows the equatorial torus and swept-back jets, along with a faint trail of diffuse X-ray emission along the radio ridge. The H.E.S.S. emission shows a peak west of J1709. This is extended toward the pulsar and a peak of emission lies to the north, within the arc of the radio shell. The faint TeV emission to the west of the radio shell may be Galactic plane background. Note that the radio

Figure 2. 6′ × 6′ composite color image of the pulsar, outflow, and jets. Red: ATCA *L*-band (1.4 GHz). Green: Chandra ACIS exposure-corrected 0.5–7 keV image, smoothed by a 2″.5 Gaussian. Blue: ATCA C-band (4.8 GHz).

emission, the TeV extension and the low surface brightness X-ray trail all coincide as a horizontal band projected across the face of the SNR arc, pointing eastwards toward J1709. We will refer to this as the pulsar wind trail.

Figure 2 shows in more detail the interaction between the outflows and the radio PWN. The radio PWN is hollow,
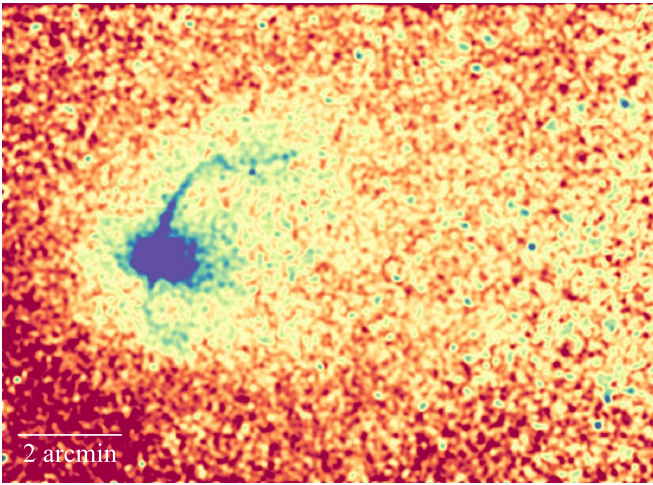
Figure 3. Exposure-corrected, 0.5–4 keV image of J1709, smoothed by a $2''5$ Gaussian. The stretch is chosen to highlight the edge of the wind bubble on the eastern side and the diffuse emission trailing the PSR on the western side.

surrounding the X-ray equatorial flow, with channels corresponding to the jets, which are swept back on arcminute scales. Figure 3 is stretched to emphasize the jet sweepback and the faint diffuse CXO emission in an east–west band. This emission ends $\theta_0 \approx 1''5$ to the east of the PSR. The overall morphology suggests an eastward pulsar velocity across this horizontally extended wind bubble with the leading edge well in front of the pulsar and the X-ray jets swept back inside. A detailed measurement of the pulsar motion can check this scenario.

3. Source Registration and Proper Motion

Given the low scintillation velocity, the proper motion shift of J1709 is expected to be a fraction of an ACIS pixel ($0''492$), even over the comparatively long baseline spanned by our data. To measure this proper motion as accurately as possible, we register the frames in each frame using the "Figure of Merit" technique ("FoM" van Etten et al. 2012; Auchettl et al. 2015; de Vries & Romani 2020). This technique compares the counts of observed registration sources on a subpixel grid, to predicted counts from simulated PSF models of those sources as a function of point-source offset, determining the source position (relative to a selected reference frame) to subpixel accuracy. We elaborate on this technique below.

One goal with the 2018–2019 ObsIDs was to cover the faint diffuse emission (and to keep the jets within read-out node boundaries). Thus in most ObsIDs, the pulsar is $>2'4$ away from the optical axis (Table 1). This led to significant PSF deformation even for the pulsar and nearby point sources. We therefore restrict our proper motion analysis to four frames in which the PSR is the closest to the optical axis: the reference frame, ObsID 4608, and 3 frames taken in late June 2018: ObsIDs 20299, 20300, and 21109. This gives us a 14.4 yr baseline over which to measure the proper motion of the pulsar.

3.1. Frame Offsets

We selected a set of registration sources based on three criteria: (1) the sources are visible in the reference frame and in at least two of the 2018 frames, (2) they do not display significant variability between the observations, and (3) they have at least $\sim$10 counts between 0.5 and 3.5 keV per

observation. Unfortunately, ObsIDs 20299 and 20300 only use three chips (S2, S3, and S4) and ObsID 21109 uses two chips (S3 and S4), limiting the number of available registration sources. We have selected a set of 14 registration sources, all of which are in the field of view in ObsIDs 04608, 20299, and 20300. For ObsID 21109, only 11 of the 14 sources fall on the ACIS chips. The sources are on average $\sim$2.5 away from the PSR, with distances ranging from $50''$ to $6'$. For each source, we looked up the hardness ratio in the Chandra Source Catalog 2.0, as well as potential optical counterparts in the Gaia DR2 catalog. Five of the sources have soft X-ray spectra, as well as an optical Gaia counterpart with known proper motion and are thus likely coronal emission from nearby field stars. We correct for the proper motions of these objects in the analysis below. The remaining nine sources have hard X-ray spectra and no detected optical counterpart. We conclude that these sources are likely to be extragalactic in origin and therefore have negligible proper motions.

For each source, we determined the reference positions in the reference frame using the CIAO tool *wavdetect*, and created spectra by extracting the counts from that source. We created one combined ACIS-S and ACIS-I spectrum for each source, fit thermal or nonthermal models to the combined spectra to create spectral models, and then computed PSF models using MARX, simulating each source for a total of 5 Ms per frame and placing the source at its reference position. The sources with known proper motions were simulated at a shifted position in the 2018 frames, by adding the Gaia proper motions (multiplied by the 14.4 yr baseline) to the 2004 reference positions. We then generated images of the MARX PSF models and data, centered on the source reference position and using a bin size of one-eighth of an ACIS pixel. We limited ourselves to counts between 0.5 and 3.5 keV to minimize effects of the particle background and the wide PSF at higher energies. Because the PSF models were all placed at the reference position, the systematic offset between the data and the source model at the center of the image should now give us the offset of the frame with respect to the reference frame.

The FoM is created by incrementally shifting the PSF model along the R.A. and decl. directions in steps of one-eighth ACIS pixel, at each step calculating the Poisson probability of the data given the model. The Poisson probability is only calculated for pixels within a circular aperture. The radius of this aperture should be large enough that sufficient counts are available for accurate centroid determination, but not so large that the FoM is significantly contaminated by background features. By calculating the frame offsets with varying aperture size, we determined that the smallest "stable" radius is around 3.5 ACIS pixel radius. Once the FoM is constructed, a 2D Gaussian function is fit to it to find the centroid and thus determine the offset of the source with respect to its reference position. To determine whether the reference positions estimated by *wavdetect* are accurate, we first constructed the FoM for the sources in the reference frame. For some of the sources, we find an offset between the *wavdetect* reference position and the FoM reference position. In these cases, we repeated the MARX simulations for that source using the new FoM reference position.

Once we verified that the FoM-determined position of each individual source in the reference frame is equal to its reference position, we added all the data and PSF models for each ObsID, and constructed a coherent FoM out of the summed data and
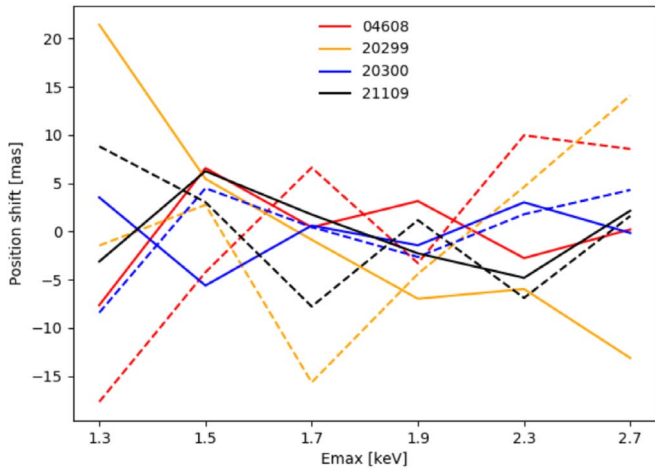
Figure 4. Positional shift in R.A. and decl. of the PSR position in different frames as a function of the upper energy bound. The lower bound of the energy range was kept constant at 0.5 keV. Solid lines indicate R.A. shifts, dashed lines indicate decl. shifts.

Table 2
Frame Shifts and Proper Motions Shown with 1σ Combined Statistical and Systematic Confidence Intervals

ObsID	Shift R.A. [10^2 mas]	Shift Decl. [10^2 mas]	$\mu_{\text{R.A.}}$ [mas yr^{-1}]	$\mu_{\text{decl.}}$ [mas yr^{-1}]
4608*	0.1 ± 0.1	0.1 ± 0.2		
20299	2.0 ± 0.3	0.2 ± 0.2	12 ± 3	-2 ± 3
20300	1.6 ± 0.3	0.4 ± 0.3	11 ± 4	-1 ± 3
21109	2.1 ± 0.4	0.6 ± 0.3	13 ± 4	1 ± 3

Note. The reference frame, ObsID 4608, is marked with an asterisk.

summed model. From this coherent FoM we then obtain the offset of the frame with respect to the reference frame.

The expected 1σ statistical uncertainty in the R.A. and decl. directions is $\sim \theta_{\text{PSF}}/N^{1/2}$, which varies from 13 to 41 mas per frame. The excess systematic error seems to depend primarily on the energy bandwidth and the aperture size used to calculate the Poisson probability at each pixel of the FoM map. In order to estimate this systematic error, we calculated the offsets of each frame with varying aperture radii, varying from 2.5 to 6 ACIS pixel radius. Based on this, we estimate the 1σ systematic uncertainty to be 20 mas.

3.2. PSR Position

To determine the position of the PSR in each frame, we proceeded as for the frame offsets. We extracted the PSR spectrum using a circular region with a $1''\!.5$ radius, then applied an aperture correction using the CIAO tool *arfcorr*. We fit a BB +PL model to the PSR spectrum, and used the resulting model fit to simulate the PSR with MARX.

The PSR is lightly affected by pileup in all observations. Using the CIAO tool *pileup_map*, we estimate the pileup fraction to be $\approx 8\%$ in the brightest pixel of the reference observation, and $\approx 7\%$ in the brightest pixel of the 2018 observations, dropping down to a few percent when averaged over the $1''\!.5$ radius extraction region. No reference source is measurably affected. We have estimated how pileup affects our results by folding the pulsar PSF simulations through the *marxpileup* tool. We determined the PSR positions in each frame using both the normal PSF and the piled up PSF. The pulsar positions change by approximately $\sim 0.3\sigma$ between the two PSFs—a shift of low significance, indicating pileup is unlikely to affect our results. We also could not detect any systematic bias in the PSR position, comparing results with the piled and unpiled PSFs.

The error on the PSR position is more likely dominated by the surrounding bright, time-variable PWN. We have attempted to minimize the effect of PWN photons by using a narrower low energy band, thereby including most of the soft, thermal PSR photons but excluding some of the harder power-law emission of the PWN. Of course, using too narrow an energy band decreases the number of available photons and therefore

increases the statistical uncertainty of the PSR position. Figure 4 shows how the PSR position shifts in R.A. and decl. for the four frames, as a function of the upper cutoff to the energy band (the lower bound was held fixed at 0.5 keV). The position shifts by ~ 15 mas. We chose an energy band of 0.5–1.7 keV as a balance between systematic and statistical errors, but it is inevitable that our choice of energy band will have some small effect on the PSR position.

A similar consideration applies for the aperture size that is used to construct the FoM. For the pulsar, we chose a comparatively small aperture size of 2 ACIS pixel radius, in order to minimize the number of PWN photons while retaining sufficient photons within the aperture for accurate statistical determination of the PSR centroid. Calculating the PSR position with different aperture sizes shows that the position estimate shifts by a similar amount (1σ uncertainty of ~ 20 mas) as a function of aperture radius. Combining these energy cut and aperture radius effects, we estimate the total 1σ systematic uncertainty to be ~ 30 mas. The statistical uncertainties were computed from the pulsar aperture counts (as for the frame offsets) and range from 8 to 14 mas.

3.3. Proper Motion

The results of the proper motion analysis and associated 1σ uncertainties per frame are listed in Table 2. We calculated the uncertainty of the proper motion in each frame by adding six terms in quadrature: the statistical uncertainties of the location of the reference star grid in the individual frame and the reference frame, the systematic uncertainty of the frame shift, the statistical uncertainties of the PSR location in the individual frame and the reference frame, and the systematic uncertainty of the PSR frame location. Averaged over all three frames, we find a proper motion $\mu_{\text{R.A.}} = 12 \pm 2 \text{ mas yr}^{-1}$ and $\mu_{\text{decl.}} = -1 \pm 2 \text{ mas yr}^{-1}$, for a total motion $\mu = 12 \pm 3 \text{ mas yr}^{-1}$.

Given the small angular velocity of J1709, local Galactic motions add a nonnegligible contribution to the true proper motion of J1709 with respect to its local environment. This proper motion is a function of (1) the differential rotation of objects orbiting in Galactic disk of the local Galactic neighborhood, as described by the Oort constants A, B, C and K, (2) the motion of the Sun with respect to its local standard of rest, described by the vectors U, V, and W, (3) the Galactic coordinates b and l of the object, and (4) the distance to the object. Using Equations (1) and (2) of Bovy (2017), the U, V, and W values of Schönrich et al. (2010), and assuming $d = 2.3$ kpc, we find that the proper motion induced by local motions is $\mu_{\text{R.A.,local}} = -0.3 \text{ mas yr}^{-1}$ and $\mu_{\text{decl.,local}} = -1.7 \text{ mas yr}^{-1}$. These numbers will increase by
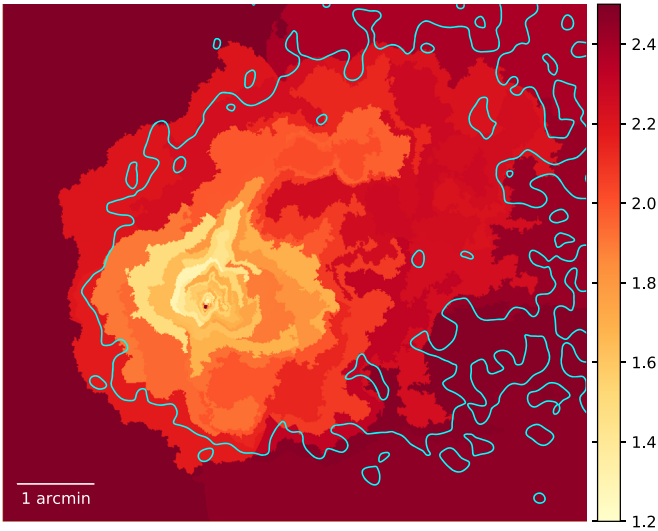
Figure 5. Photon index map of J1709. Spectral bins were defined following surface brightness contours. To the spectrum extracted from each bin, we fit a PL model with N_H set to 5×10^{21} cm^{-2}. The typical 90% error is 0.11. The edge of the wind bubble (see Figure 3) is shown as the cyan contour.

Figure 6. Adaptively smoothed image of J1709, showing spectral extraction regions with solid lines and regions used for background subtraction with white dashed lines.

$\approx$10% at $d = 2$ kpc, or decrease by $\approx$20% at $d = 3$ kpc, well below the 1σ uncertainty on J1709's proper motion in either case.

Correcting for the local proper motion shifts the true proper motion vector to $\mu_{\mathrm{R.A.}} = 13 \pm 2$ mas yr^{-1}, and $\mu_{\mathrm{decl.}} = 1 \pm 2$ mas yr^{-1}, for a total motion of $\mu = 13 \pm 3$ mas yr^{-1} at a PA of $86 \pm 9°$. The final proper motion vector, extrapolated backwards for the 1.7×10^4 yr spindown age, is shown in Figure 1. At $d = 2.3$ kpc, our measured proper motion corresponds to a 2D velocity $v_t = 136 \pm 30$ km s^{-1}. This is larger than the scintillation velocity estimate $v_t \approx 90$ km s^{-1} (Johnston et al. 1998), suggesting that the scattering screen dominating the scintillation is closer than halfway to Earth or that the pulsar distance is <2 kpc.

4. Spectral Analysis

4.1. Photon Index Map

We have constructed a photon index map of J1709 and its immediate surroundings by making bins with the *contbin* algorithm (Sanders 2006), often used to map the thermal properties of the intracluster medium in galaxy clusters. This algorithm constructs bins of approximately equal S/N, with bins following the surface brightness contours of the input data. We analyzed a region of $450 \times 400''$, covering the PSR, PWN, the swept-back jets, and some of the diffuse X-ray emission trailing the system. Using an S/N of 25, we obtained 96 bins for which we extracted spectra using the CIAO tool *specextract*. We used the ACIS blank-sky files as the background. For each region, we created a combined ACIS-S and a combined ACIS-I spectrum using *combine_spectra*. We then fit an power-law model to these spectra, setting the Galactic column density of N_H to the value determined by Romani et al. (2005), $N_H = 5 \times 10^{21}$ cm^{-2}. The resulting map is shown in Figure 5.

In general, the photon index in the innermost regions is comparable to what is observed in other bright, spatially resolved PWNe (Kargaltsev et al. 2017), albeit on the harder
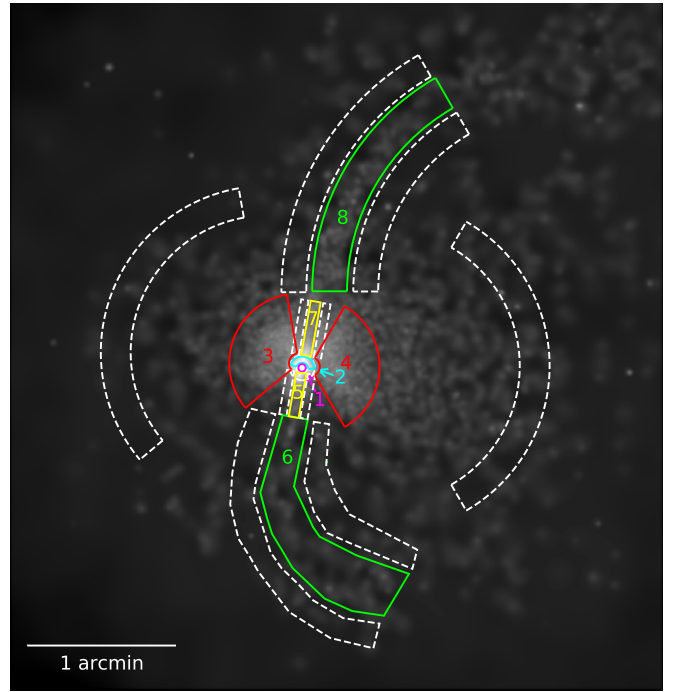
side. The spectrum softens with increasing distance from the PSR because of synchrotron losses. On the eastern side of the PWN equatorial outflow, where the torus is compressed by ram pressure, we observe a few bins where the spectrum appears to be harder than the rest of the PWN, $\Gamma \approx 1.3$, and an inner arc on the eastern side appears even harder. These bins wrap around toward the jet which, in the north, also reveals particularly hard emission. The connection with the jets may explain the nonmonotonic increase in Γ with distance from the PSR. We also see a clear division between the emission inside and outside the pulsar wind bubble, with the emission inside the bubble being harder than the $\Gamma \approx 2.5$ background.

4.2. Spectral Fits of Specific Features

In addition to the photon index map, we have extracted the spectra from several individual features, which are shown in Figure 6. For these fits we subtracted a local background spectrum, rather than using an ACIS "blank-sky" background. For the PSR, we assume that the emission is generated by a combination of thermal emission from the surface, as well as power-law emission from the magnetosphere. We therefore fit a composite blackbody + power law model to the PSR spectrum. For the other regions, we assume a simple synchrotron power-law spectrum. The Galactic absorption is again set to $N_H = 5 \times 10^{21}$ cm^{-2}. The results of these fits are listed in Table 3. These fits show similar trends to those observed in Figure 5, including a clear asymmetry between the eastern and western sides of the PWN. Additionally, we note that for the inner jet region, the ACIS-S and ACIS-I combined spectra show different values of Γ when fit individually, $\Gamma = 1.55 \pm 0.22$ and $\Gamma = 1.33 \pm 0.14$, respectively. The difference is barely significant, but it may be the result of month-timescale jet variability, as seen in Figure 7.

Table 3
Spectral Fit Results of Regions Shown in Figure 6, with 0.5–7 keV Unabsorbed Fluxes for Each Spectral Model, and 90% Confidence Intervals for All Parameters

Nr	Comp	Counts	$f_{0.5-7\ keV}$ [erg cm^{-2} s^{-1}]	kT/Γ [keV]/	χ^2/DoF
1	PSR (BB)	15551 ± 129	$(4.13 \pm 0.16) \times 10^{-13}$	0.180 ± 0.004	240/226
1	PSR (PL)	$''$	$(2.17 \pm 0.09) \times 10^{-13}$	1.46 ± 0.09	$''$
2	Torus	5371 ± 75	$(1.26 \pm 0.03) \times 10^{-13}$	1.46 ± 0.05	216/211
3	PWN E	5283 ± 82	$(1.25 \pm 0.05) \times 10^{-13}$	1.49 ± 0.06	235/254
4	PWN W	5627 ± 87	$(1.35 \pm 0.05) \times 10^{-13}$	1.61 ± 0.06	184/188
5	Inner jet	1657 ± 49	$(3.9 \pm 0.2) \times 10^{-14}$	1.41 ± 0.11	159/185
6	Outer jet	594 ± 65	$(1.4 \pm 0.4) \times 10^{-14}$	1.47 ± 0.53	107/105
7	Inner c/jet	1242 ± 54	$(2.9 \pm 0.3) \times 10^{-14}$	1.23 ± 0.18	129/195
8	Outer c/jet	1211 ± 65	$(2.8 \pm 0.2) \times 10^{-14}$	1.33 ± 0.24	119/126

Note. The Galactic absorption was held fixed at $N_H = 5 \times 10^{21}$ cm^{-2}. The PSR region was fit with a composite blackbody + power law model, all other regions were fit with a power-law model.
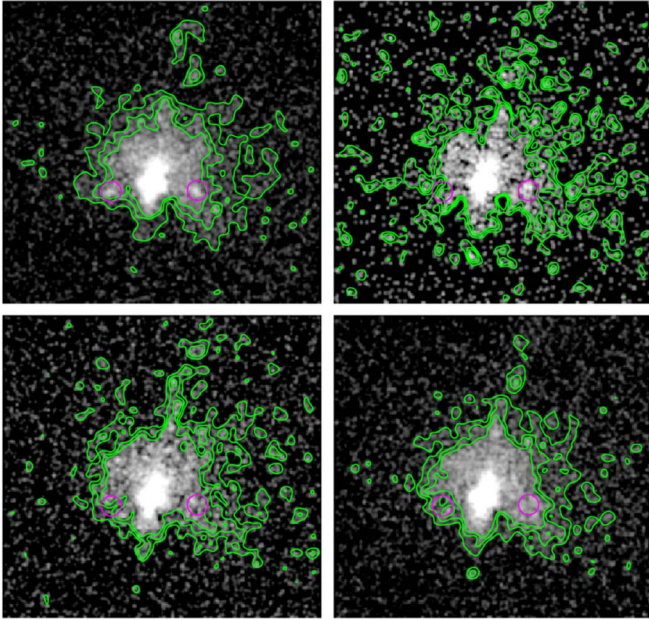
Figure 7. Exposure-corrected images of J1709: epoch 3 (top left), 4 (top right), 5 (bottom left), and 6 (bottom right). Surface brightness contours are shown in green, to emphasize the jet variability between epochs. The PWN spots (primarily visible in epoch 3) are marked with magenta circles.

We can use these spectral measurements to estimate the magnetic field strength in the synchrotron-emitting PWN components. For an optically thin region filled with relativistic electrons and magnetic field emitting synchrotron radiation

$$B = 46 \left[\frac{J_{-20}(E_1, E_2)\sigma}{\phi} \frac{C_{1.5-\Gamma}(E_m, E_M)}{C_{2-\Gamma}(E_1, E_2)} \right]^{2/7} \mu G, \qquad (1)$$

where

$$C_q(x_1, x_2) = \frac{x_2^q - x_1^q}{q}. \qquad (2)$$

$J_{-20}(E_1, E_2) = 4\pi f_{-20}(E_1, E_2)d^2/V$ is the observed emissivity (in 10^{-20} erg s^{-1} cm^{-3}, between E_1keV and E_2keV), $\sigma = w_B/w_e$ is the magnetization parameter, ϕ is the filling factor, and E_m and E_M are the minimum and maximum energies of the power-law Γ synchrotron spectrum, in keV.

For the inner jet and inner counterjet, we use the fluxes from Table 3, and estimate the jet volume as a cylinder inclined

$\sim 37°$ from the sky plane. If we assume $\sigma = 1$, a distance $d = 2.3$ kpc, $\phi = 1$ and that the photon spectrum extends from $1\ \mathrm{eV} - 1\ \mathrm{MeV}$, we obtain $B = 43\ \mu$G for the inner jet and $B = 40\ \mu$G for the inner counterjet.

For the PWN, we divided regions 3 and 4 into inner and outer parts with equal radius. We estimated the volume of these regions as spherical shells projected along the line of sight. Using the same assumptions as for the jet and counterjet, we estimate that $B = 27\ \mu$G for the inner PWN, and $B = 15\ \mu$G for the outer PWN. These are rough estimates only, as the jet clumping suggests $\phi < 1$ and multiwavelength data at present provide little constraint on the full spectral range.

5. The Variable Jets and PWN

We have divided the total CXO data set of J1709 into six different epochs: (1) 2000 [15 ks], (2) 2004 [99 ks], (3) 2018 June [230 ks], (4) 2018 October [53 ks], (5) 2019 January–February [173 ks], (6) 2019 May–June [216 ks]. Closer inspection of the system at these different epochs reveal some interesting structural variation. In epoch 3, two bright spots appear in the outflow, roughly equidistant east and west from the PSR. Exposure-corrected images for epochs 3, 4, 5, and 6 are shown in Figure 7. The spots are statistically significant, with an S/N ratio of 5.6 for the eastern spot and 6.0 for the western spot. Unfortunately, the subsequent epoch 4 is limited by poor count statistics as the observations were interrupted by CXO going into safe mode. The western spot appears still visible at the same location in this epoch, at an S/N ratio of 3.6.

We have extracted spectra from the spots, but a detailed analysis is difficult with the limited number of counts and low contrast with the surrounding PWN. For the eastern spot, a background-subtracted spectrum (using a background annulus directly around the spot) results in a spectrum with 68 counts between 0.7 and 6 keV. Fitting an absorbed PL with $N_H = 5 \times 10^{21}$ cm^{-2} yields a photon index of 1.35 ± 0.67. For the western spot, we obtain 97 counts and a photon index of 1.15 ± 0.46. While nominally harder than the surrounding torus/outflow emission, the difference is not statistically significant.

The jets of J1709 also seem to show variability in different epochs, somewhat reminiscent of the variable jet in the Vela Pulsar (Pavlov et al. 2003). In particular, there seems to be some side-to-side instability in the jet axis in epoch 5. However, on a larger scale the jets are remarkably narrow and curve smoothly, apparently swept back by flow within the
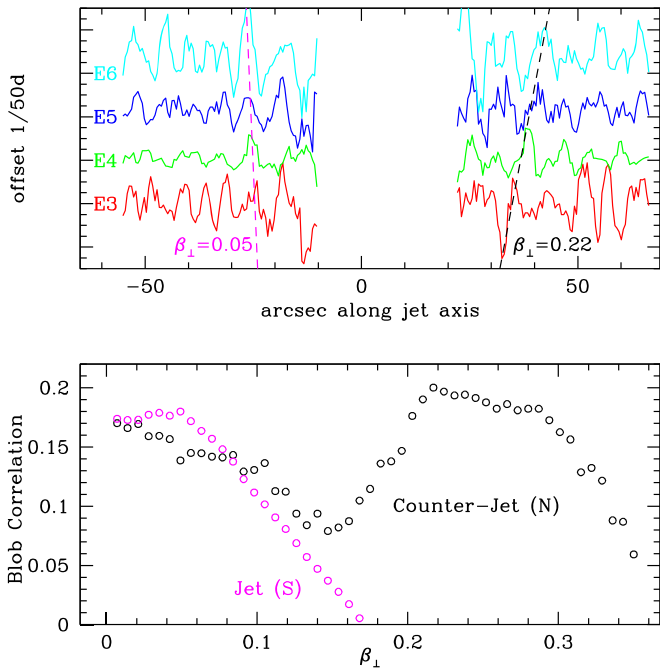
Figure 8. Top panel: count profiles along the jet axis for epochs 3, 4, 5, and 6. These profiles are offset vertically by one tick mark/50 days between epochs. The x-axis direction is south (jet) to north (counterjet). Bottom panel: result of the cross-correlation for jet and counterjet, suggesting blob motions $\beta_\perp \approx 0.05$ for the jet, and $\beta_\perp \approx 0.22$ for the counterjet.

pulsar wind bubble. The limited jet spread implies some source of continuous recollimation (possibly magnetic hoop stress). We also attempted to analyze intra-epoch jet blob motion by using a cross-correlation routine to compare count profiles along the jet axis at different epochs, as shown in Figure 8. This showed little lagged correlation in the southern (jet) source, consistent with $\beta_\perp = v_\perp/c < 0.05$. For the northern (counter-) jet, a broad correlation peak suggests $\beta_\perp \approx 0.22$. However, no epoch showed bright stable blobs, and we fear that the significance of these correlations is difficult to quantify. Thus we will not use these β values to draw physical conclusions.

6. Discussion and Conclusions

Armed with a direct proper motion measurement, we can re-evaluate the association of PSR J1709−4429 with SNR G343.1−2.3. The ∼25′ radius radio arc has been proposed by Bock & Gvaramadze (2002) to be the interaction of the blastwave with a molecular cloud, with the balance of the shell 3–4× larger, faint or invisible in a less-confined region to the east. These authors require a proper motion 35 mas yr^{-1} to the SE to bring the PSR to its present location in the spindown age. In contrast, our proper motion is ∼3× smaller, nearly due east, so birth at the center of the radio arc is excluded. On the other hand, few pulsars as young as 17 kyr lack parent supernova remnants, and with the low proper motion guaranteed for J1709, G343.1−2.3 is the only candidate in the vicinity.

If, instead, the birthsite is 17 kyr back along our proper motion vector (base of the magenta arrow in Figure 1) the explosion was ∼8′ south of the center of the radio arc. One might infer that the pulsar progenitor traveled south toward this point, evacuating a cavity via a strong stellar wind. Explosion into this cavity led to the offset (but surprisingly symmetric)

radio arc seen today. In response to this explosion the pulsar now travels east at ∼90° to its progenitor's motion.

We have noted that the combined radio/X-ray/TeV trail matches well with the proper motion axis and terminates in a rounded front centered on the pulsar. This can be interpreted as a trailed PWN. In this picture it is natural to associate the TeV peak (Hoppe et al. 2009) with "remnant" electrons marking the pulsar's rapid initial spindown, while the X-ray trail following the torus and jets represent younger, higher energy electrons. However, we would require ∼5 × τ_c ≈ 85 kyr (cyan arrow in Figure 1) for travel from the TeV peak. An alternative origin for the TeV emission is G343.1−2.3-generated cosmic rays interacting with the dense gas marking the remnant's western boundary at the radio arc. Indeed the lobe of TeV emission extending north into the radio arc supports this interpretation for at least part of the flux. However, the extension toward the pulsar argues that at least some of the TeV emission is associated with J1709. The faint lobe to the west may be insignificant or background from the Galactic plane. The improved spectral imaging expected with the Cherenkov Telescope Array may be able to address the origin of this TeV emission.

It is relatively common for young pulsars to have spindown ages τ_c in excess of their kinematic ages, e.g., indicating a large spin period at birth. There are only a few PSR for which the opposite has been suggested. Perhaps the most discussed example is the PSR B1757−24/G5.4−1.2 association ("the Duck"), where the upper limit on the proper motion requires a true age of >4 × τ_c for the association to be real (Zeiger et al. 2008). One way to reconcile such age differences is late time growth of the magnetic field (Blandford & Romani 1988) or magnetic geometry changes that increase the braking torque within the past ∼τ_c. A similar argument might apply to J1709, although one would require a large field near birth if the high energy deposition at the TeV maximum is to be explained. One could then speculate that the spindown torque oscillates, e.g., due to free precession on a timescale of a few τ_c. If the pulsar really were born at the current location of the TeV peak at the edge of the radio shell, the required extreme asymmetry of the remnant expansion would be very difficult to understand. Of course, if the true age is ⩾85 kyr, it is also easier for the parent SNR to have faded below visibility, and so the association with G343.1−2.3 might not be required in this scenario.

Interpreting the X-ray/radio/TeV horizontal band as a PWN trail, it is of interest to understand why this region extends $\theta_0 \sim 90''$ in front of the pulsar. One possibility is that this is a classical bow shock, set by momentum balance between the pulsar wind and the ram pressure of the external medium, with

$$\theta_0 = [\dot{E}/(4\pi c\rho v^2)]^{1/2}/d$$
$$= 150''[\dot{E}_{36}\sin^2 i/n_p \mu_{mas/y}^2]^{1/2} d_{kpc}^{-2}. \quad (3)$$

This applies when the pulsar motion is supersonic in the external medium. For such a large standoff J1709's low proper motion helps, but we would also need a low external density $n_p \approx 2.5 \times 10^{-3}(d/2.3\,{\rm kpc})^{-4}\,{\rm cm}^{-3}$. Such low densities can occur in stellar wind bubbles or supernova remnants, but with long cooling times the temperatures and pressures in such cavities would be too high for the pulsar motion to be supersonic.

The standoff may instead be controlled by energy balance for a subsonic pulsar. Here the pulsar wind bubble expands in a

Sedov-like solution to

$$R(t) = [1.3\dot{E}t^3/\rho]^{1/5} = 0.6(\dot{E}_{36}/n_p)^{1/5}t_3^{3/5} \text{ pc}, \quad (4)$$

where t_3 is a characteristic energy deposition time, in units of 10^3 yr. The leading edge of this wind bubble holds steady at the present standoff when the expansion velocity

$$v(t) = \dot{R}(t) = 352(\dot{E}_{36}/n_p)^{1/5}t_3^{-2/5} \text{ km s}^{-1} \quad (5)$$

balances the pulsar motion, with ratio $R/v = 1670t_3$yr. Observationally, $R/v \approx 7{,}200$ yr so we infer $t_3 \approx 4.3$, that is to say that the effective confinement time of the pulsar wind is $\sim$4,300 yr with the relativistic $e^\pm/B$ plasma venting behind the pulsar, to the west. For this timescale and the pulsar spindown power we infer a density $n \approx 0.084d_{2.3}^{-5}\dot{E}_{36}t_3^3$ cm$^{-3} \approx 27$ cm^{-3} from the wind bubble standoff with the nominal confinement time, or ≈ 0.34 cm^{-3} for more efficient wind venting with $t_3 \sim 1$. Given the proximity to the Galactic plane and evidence for molecular gas west of G343.1−2.3, a large density does not seem unreasonable if the pulsar is not embedded in the SNR, although it would likely require some pulsar motion out of the plane of the sky to escape to a dense external medium. This wind venting is appealing as it provides a natural source of the backflow that sweeps the jets back toward the pulsar tail, with speeds several times $v_{\rm PSR}$. In addition, the venting PWN trail will sweep partly cooled $e^\pm$ to the west, perhaps even beyond the pulsar birthsite to the TeV peak, mitigating the disagreement with the characteristic age.

The torus and jets themselves can be related to the proper motion. Romani et al. (2005) fit the torus/jet axis at a position angle 164°, some 77° from the proper motion axis. In addition the relativistic torus fit implies the (southern) jet axis projects $\sim$37° out of the plane of the sky. If we assume a proper motion within the plane of the sky, then the jet (pulsar spin) axis lies $\sim$80° from the proper motion vector. In Ng & Romani (2007) it was found that when both spins and proper motions are introduced by a natal kick, low-velocity objects have the highest probability of large spin-velocity angles.

Note that the southern jet is pointing against the venting wind flow and is truncated. If the 3D space velocity has a component out of the plane of the sky, then this jet would be pointing somewhat closer to the forward direction. This should enhance the backflow asymmetry with the northern counterjet, which sweeps back and fades smoothly into the PWN trail. Thus 3D relativistic MHD simulations following the polar field lines of the jet and counterjet might be able to constrain the 3D space motion, and by constraining the venting flow speed can determine the upstream density and the distance traveled by the TeV emitting $e^\pm$.

We conclude the PSR J1709 was not born at the center of SNR G343.1−2.3, but instead the explosion occurred somewhere between its present position and the TeV peak. If the true age is $\sim\tau_c$, then the SNR association is plausible, but requires progenitor motion, substantial expansion asymmetry, a birth kick nearly orthogonal to this asymmetry and substantial flow of the PWN $e^\pm$ (if these cause the TeV emission). Alternatively, if born at the TeV peak $\sim 5\tau_c$ ago, then the required explosion symmetry is even more extreme. This places the association in doubt, but does allow more time for a hypothetical older birth SNR to fade.

Tunneling into a relatively dense medium, the pulsar is evacuating a wind-blown trail, whose relativistic shocked $e^\pm/B$ fluid is venting to the west. The bubble scale suggests a bulk outflow speed $>4 \times v_{\rm PSR}$. This flow is graphically displayed by the jets that mark the polar axis field lines of the PWN outflow. These remain relatively well collimated, but are swept to the west on a timescale shorter than the pulsar crossing time. The high spindown power (and relatively low pulsar velocity) guarantee that the jets and torus are not crushed as in some older pulsar bow shocks. In this picture the jet sweepback is not a direct effect of the pulsar motion, but rather a secondary effect of its (motion-induced) tunneling into a dense medium with backflow escaping behind the pulsar and sweeping the jets along with this venting wind. Simulations are needed to see if this picture is viable and to further constrain the flow speed.

ORCID iDs

Martijn de Vries ● https://orcid.org/0000-0001-5282-0404
Roger W. Romani ● https://orcid.org/0000-0001-6711-3286
Oleg Kargaltsev ● https://orcid.org/0000-0002-6447-4251
George Pavlov ● https://orcid.org/0000-0002-7481-5259
Patrick Slane ● https://orcid.org/0000-0002-6986-6756
Niccolo' Bucciantini ● https://orcid.org/0000-0002-8848-1392
C.-Y. Ng ● https://orcid.org/0000-0002-5847-2612
Noel Klingler ● https://orcid.org/0000-0002-7465-0941

References

Auchettl, K., Slane, P., Romani, R. W., et al. 2015, ApJ, 802, 68
Blandford, R. D., & Romani, R. W. 1988, MNRAS, 234, 57P
Bock, D. C. J., & Gvaramadze, V. V. 2002, A&A, 394, 533
Bovy, J. 2017, MNRAS, 468, L63
Cordes, J. M., & Lazio, T. J. W. 2002, arXiv:astro-ph/0207156
de Vries, M., & Romani, R. W. 2020, ApJL, 896, L7
Dodson, R., & Golap, K. 2002, MNRAS, 334, L1
Gotthelf, E. V., Halpern, J. P., & Dodson, R. 2002, ApJL, 567, L125
H.E.S.S. Collaboration, Abdalla, H., Abramowski, A., et al. 2018, A&A, 612, A1
H.E.S.S. Collaboration, Abramowski, A., Acero, F., et al. 2011, A&A, 528, A143
Hoppe, S., de Oña-Wilhemi, E., Khélifi, B., et al. 2009, arXiv:0906.5574
Johnston, S., Lyne, A. G., Manchester, R. N., et al. 1992, MNRAS, 255, 401
Johnston, S., Nicastro, L., & Koribalski, B. 1998, MNRAS, 297, 108
Kargaltsev, O., Klingler, N., Chastain, S., & Pavlov, G. G. 2017, JPhCS, 932, 012050
McAdam, W. B., Osborne, J. L., & Parkinson, M. L. 1993, Natur, 361, 516
Ng, C. Y., & Romani, R. W. 2004, ApJ, 601, 479
Ng, C. Y., & Romani, R. W. 2007, ApJ, 660, 1357
Pavlov, G. G., Teter, M. A., Kargaltsev, O., & Sanwal, D. 2003, ApJ, 591, 1157
Romani, R. W., Ng, C. Y., Dodson, R., & Brisken, W. 2005, ApJ, 631, 480
Sanders, J. S. 2006, MNRAS, 371, 829
Schönrich, R., Binney, J., & Dehnen, W. 2010, MNRAS, 403, 1829
van Etten, A., Romani, R. W., & Ng, C. Y. 2012, ApJ, 755, 151

Zeiger, B. R., Brisken, W. F., Chatterjee, S., & Goss, W. M. 2008, ApJ, 674, 271